AGU PUBLICATIONS

JGR

Journal of Geophysical Research: Planets

RESEARCH ARTICLE
10.1002/2014JE004734

Key Points:
- A new method to model partially distributed magnetic field measurements
- Method applied to Mercury's field observed by MESSENGER's eccentric orbit
- We find a strongly axisymmetric internal field

Supporting Information:
- Supporting Information S1
- Software S1

Correspondence to:
J. S. Oliveira,
joana.oliveira@univ-nantes.fr

Citation:
Oliveira, J. S., B. Langlais, M. A. Pais, and H. Amit (2015), A modified Equivalent Source Dipole method to model partially distributed magnetic field measurements, with application to Mercury, *J. Geophys. Res. Planets*, *120*, doi:10.1002/2014JE004734.

Received 1 OCT 2014
Accepted 11 MAY 2015
Accepted article online 15 2015

©2015. American Geophysical Union. All Rights Reserved.

A modified Equivalent Source Dipole method to model partially distributed magnetic field measurements, with application to Mercury

J. S. Oliveira[1,2], B. Langlais[1], M. A. Pais[2,3], and H. Amit[1]

[1]Laboratoire de Planétologie et Géodynamique, LPG Nantes, CNRS UMR6112, Université de Nantes, Nantes, France, [2]CITEUC, Geophysical and Astronomical Observatory, University of Coimbra, Coimbra, Portugal, [3]Department of Physics, University of Coimbra, Coimbra, Portugal

Abstract Hermean magnetic field measurements acquired over the northern hemisphere by the MErcury Surface Space ENvironment GEochemistry, and Ranging (MESSENGER) spacecraft provide crucial information on the magnetic field of the planet. We develop a new method, the Time Dependent Equivalent Source Dipole, to model a planetary magnetic field and its secular variation over a limited spatial region. Tests with synthetic data distributed on regular grids as well as at spacecraft positions show that our modeled magnetic field can be upward or downward continued in an altitude range of −300 to 1460 km for regular grids and in a narrower range of 10 to 970 km for spacecraft positions. They also show that the method is not sensitive to a very weak secular variation along MESSENGER orbits. We then model the magnetic field of Mercury during the first four individual sidereal days as measured by MESSENGER using the modified Equivalent Source Dipoles scheme and excluding the secular variation terms. We find a dominantly zonal field with small-scale nonaxisymmetric features corotating with the Sun in the Mercury Body Fixed system and repeating under similar local time, suggestive of external origin. When modeling the field during one complete solar day, these small-scale features decrease and the field becomes more axisymmetric. The lack of any coherent nonaxisymmetric feature recovered by our method, which was designed to allow for such small-scale structures, provides strong evidence for the large-scale and close-to-axisymmetry structure of the internal magnetic field of Mercury.

1. Introduction

The discovery of a magnetic field of internal origin on Mercury during the Mariner 10 mission flybys [*Ness et al.*, 1974, 1975] was a surprise. Because of Mercury's small size, it was thought that its interior was completely solidified, with no liquid core capable of sustaining a dynamo [*Plagemann*, 1965]. But the observed planetary scale of the Hermean magnetic field argues for a deep core dynamo origin. This hypothesis is supported by analyses of the gravity field and of planetary spin parameters from both Earth-based radar and MErcury Surface Space ENvironment GEochemistry, and Ranging (MESSENGER) radio science measurements, which show that the metallic core of Mercury is at least partially molten [*Margot et al.*, 2007; *Smith et al.*, 2012].

Previous studies have shown a weak intensity of Mercury's magnetic field, about 1% of the Earth's [*Ness et al.*, 1974; *Anderson et al.*, 2008], suggesting that the Hermean dynamo works differently. Numerical dynamo studies suggest that the planetary magnetic field magnitude is not necessarily determined by a magnetostrophic force balance (i.e., between Coriolis, Lorentz, and pressure forces) but instead by the buoyancy flux, with Elsasser numbers varying substantially from 0.06 to 100 [*Christensen and Aubert*, 2006]. Given the estimated field intensity at Mercury's core surface ($\sim 10^{-4}$ mT), the Elsasser number would be on the order of 10^{-4}, well below the lower bound found by *Christensen and Aubert* [2006]. To obtain such a low Elsasser number, numerical dynamos should incorporate less Earth-like special effects, such as stratification at the top of the core [*Christensen*, 2006; *Christensen and Wicht*, 2008] or iron snow zone at mid shell [*Vilim et al.*, 2010].

Characterizing the origin and the nature of the Hermean magnetic field are two of the main scientific objectives of the NASA MESSENGER mission [*Solomon et al.*, 2001] that has been in orbit since March 2011. The spacecraft orbits around Mercury on a very eccentric trajectory, with an initial 200 km altitude periapsis set at 60°N latitude. Because of this very eccentric orbit, only when the satellite flies above the northern

hemisphere it reaches an altitude low enough so that the magnetic field of internal origin can be constrained by its magnetometer (MAG) instrument [*Anderson et al.*, 2007].

The first analyses of MESSENGER's magnetic field measurements were based on a simple approach as far as the internal part is concerned. *Anderson et al.* [2011, 2012] found that the magnetic equator (where the cylindrical radial field vanishes) is located in the northern hemisphere, with an offset of 0.196 R_M where R_M = 2440 km is Mercury's radius. A weak magnetic moment of 190 nT R_M^3 was obtained via a grid search by *Johnson et al.* [2012], in agreement with previous estimates based on Mariner 10 measurements [*Ness et al.*, 1974, 1975]. The location of the magnetic equator at the northern hemisphere motivated modeling the internal field with a simple offset dipole. The estimated dipole offset corresponds to an axial quadrupole to axial dipole ratio of $g_2^0/g_1^0 = 0.392 \pm 0.010$ [*Anderson et al.*, 2012]. In addition, these studies found that the dipole tilt is very small, with an upper limit placed at 0.8°. The offset dipole internal field model in these studies permitted a simultaneous evaluation of large-scale external fields. Finally, a recent study attempted to detect the secular variation (SV) of Mercury's field by comparing MESSENGER and Mariner 10 data [*Philpott et al.*, 2014]. It was found that the analyzed data are consistent with no SV, although some variations in the lowest zonal spherical harmonics (SH) coefficients are possible.

Parametric studies of numerical dynamo models found two main types of solutions: when convection is vigorous and rotational effects are moderate, a large g_2^0/g_1^0 ratio may be found but a large nonzonal field is also present; when convection is moderate and rotational effects are vigorous, a small nonzonal field is found but the g_2^0/g_1^0 ratio is also small [*Kutzner and Christensen*, 2002; *Christensen and Aubert*, 2006]. Heterogeneous core-mantle boundary (CMB) heat flux can help to obtain a large g_2^0/g_1^0 ratio together with small nonzonal terms, as was applied to the paleo-dynamo of Mars [*Stanley et al.*, 2008; *Amit et al.*, 2011; *Dietrich and Wicht*, 2013], but there is no solid evidence for hemispheric mantle heterogeneity in Mercury. The large g_2^0/g_1^0 ratio found by *Anderson et al.* [2012] together with the very axisymmetric field are therefore challenging constraints for Mercury dynamo models [*Cao et al.*, 2014; *Wicht and Heyner*, 2014].

Previous models of the Hermean internal magnetic field do not take full advantage of the available measurements as they contain no information on smaller spatial scale features. The standard spherical harmonics (SH) approach is commonly used to represent the global geomagnetic field and is especially appropriate when the data coverage is global [*Cain et al.*, 1989]. For other planets or bodies, where measurements are much more sparse and only partially distributed, SH may also be applied when additional constraints or regularizations are imposed [*Connerney et al.*, 1987, 1991; *Holme and Bloxham*, 1996]. Alternatively, local methods such as the spherical cap harmonic analysis [*Thébault et al.*, 2006] may be employed to describe an internal magnetic field measured with a partial planetary coverage. In the case of magnetic field of lithospheric origin, continuous or discrete magnetization models can also be computed [*Langlais et al.*, 2004; *Whaler and Purucker*, 2005].

In this study we choose to adapt an existing discrete source method, the Equivalent Source Dipole (ESD) scheme initially developed for the crustal geomagnetic field [e.g., *Mayhew*, 1979], to model the Hermean field. Our method uses MESSENGER's partial data coverage without employing arbitrary constraints or regularizations. We implement the method to analyze measurements acquired by MESSENGER spacecraft orbiting Mercury, reaching low altitudes over an area of limited extent.

We modify the ESD scheme for purposes of internal core field modeling. The two main modifications with respect to ESD consist in using deep dipole sources and a linear time dependency for the dipole parameters. We term this the Time-Dependent Equivalent Source Dipole (TD-ESD) method.

We present in section 2 the theoretical foundations of the method. In section 3 we explain the modeling technique and how solutions are chosen. Then in section 4 the method is tested and validated with synthetic magnetic field data for both ideal and realistic cases. These tests include dependencies on horizontal resolution, depth of the dipoles mesh, and noise effect. In addition, we test the range of possible downward/upward continuation. In section 5 we show the first maps of Mercury's magnetic field components derived using our modified ESD method. In section 6 we discuss our results and compare with previous studies. Finally, in section 7 we summarize our main findings.

2. Theory

The Time-Dependent Equivalent Source Dipole method is an extension of the Equivalent Source Dipole method. The ESD method applied to magnetism was introduced by *Emilia* [1973]. It initially aimed at reducing, to a common altitude, magnetic field anomaly measurements of lithospheric origin acquired at various altitudes [*Mayhew*, 1979; *von Frese et al.*, 1981; *Purucker et al.*, 1996; *Dyment and Arkani-Hamed*, 1998]. It is commonly used to produce global lithospheric magnetic field maps of the Earth [*Purucker et al.*, 1998], Mars [*Langlais et al.*, 2004], and Moon [*Purucker et al.*, 2012] and may be applied to local data coverage [*Purucker et al.*, 2002; *Langlais and Purucker*, 2007].

In the ESD method, the magnetic field measured at a given location results from individual contributions by dipolar sources located at some depth. The magnetic potential due to a single source is given by

$$V = -\frac{\mu_0}{4\pi}\mathbf{M}\cdot\nabla\frac{1}{l} \tag{1}$$

where $\mathbf{M}$ is the magnetization of the dipole located at spherical coordinates radius, colatitude, and longitude (r_d, θ_d, ϕ_d). The magnetic field depends on the magnetic potential through $\mathbf{B} = -\nabla V$. The distance between the dipole and the observation point at (r, θ, ϕ) is

$$l = \sqrt{r_d^2 + r^2 - 2r_d r\left(\cos\theta\cos\theta_d + \sin\theta\sin\theta_d\cos\left(\phi - \phi_d\right)\right)} \tag{2}$$

For the ESD approach the dipole sources are placed at the surface of the planet or a few kilometers below [*Langlais et al.*, 2004], because the lithospheric magnetic field has a shallow origin. Here, for the TD-ESD method, the dipole sources are placed at a spherical surface deep inside the planet's interior in order to model the magnetic field of core origin. In addition, we may let the magnetization vary in time, as the core field is also time dependent. This is done through

$$\mathbf{M}(t) = \mathbf{M}(t_0) + (t - t_0)\dot{\mathbf{M}} \tag{3}$$

where $\mathbf{M}(t_0)$ is the magnetization at a reference time t_0 and $\dot{\mathbf{M}}$ is its rate of change. We assume that the time dependence is linear. This approximation may be too simplistic to model the field variations associated with core dynamics. We, however, note that using a more complex parameterization would not change the concept of the approach and can be considered in the future if necessary. The TD-ESD method thus simultaneously describes the three observed magnetic field components B_r, B_θ, and B_ϕ as being due to an internal distribution of the three magnetization components M_r, M_θ, and M_ϕ and the three components of its time variation rate. This new method, therefore, requires fitting six parameters at each dipole position instead of three as in the original ESD method.

3. Method

3.1. Spatial Resolution

The method searches for magnetization components and their variation rate for each dipole. These dipoles are located on an equisurface and equidistant mesh deep inside the planet at a depth R_d. We use the polar coordinate subdivision method [*Katanforoush and Shahshahani*, 2003] for distributing the dipole sources. The spherical surface is divided into n_d equally spaced latitude bands, where n_d is the dipole mesh parameter. At colatitude θ_j, where $\theta_j = \pi - \frac{\pi j}{(n_d+1)}$ and $j = 1, \ldots, n_d$, we place N_j equally spaced dipoles, where N_j is the integer of n_j, the latter given by

$$n_j = \left[\frac{1}{2} + \sqrt{3}(n_d + 1)\sin\theta_j\right]. \tag{4}$$

At alternate latitudes, a longitudinal phase shift is imposed to render the mesh more homogeneous. The relation between n_d and the total number of dipoles on the sphere N_{dip} is shown in Figure 1. Increasing n_d corresponds to increasing N_{dip} and to decreasing the mean spacing d between adjacent dipoles, leading to a better spatial resolution. Figure 2 shows an example of a dipole mesh with $n_d = 15$. In the following we assume that each dipole is assigned to a horizontal circular surface and that its associated magnetization is confined to a 10 km vertical layer. The choice of thickness affects the magnitude of the magnetization (which is not given any physical interpretation) but not the magnitude of the magnetic field, so this choice is not critical [*Purucker et al.*, 2012].

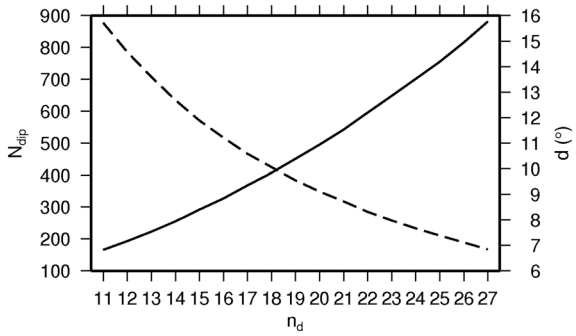

Figure 1. Total number of dipoles N_{dip} (solid line) and the mean distance between adjacent dipoles in degrees d (dashed line) as a function of the dipole mesh parameter n_d.

3.2. Inversion and Model Evaluation

The inverse problem is written as

$$\mathbf{b} = D\mathbf{x} + \nu \tag{5}$$

where **b** is the column vector containing the magnetic field components, **x** is the column vector containing the magnetization and rate of change components, and D is the matrix containing the partial derivatives relating **b** to **x**; ν is the error vector. The magnetic field due to an individual dipole is proportional to $1/l^3$ so observations too far away from a given dipole do not constrain its magnetization. As a result, the matrix D is sparse [e.g., *Purucker et al.*, 1996] and includes only elements for which the observation-to-dipole distance is less than a threshold value or when the angle between the observation point and the dipole is less than 90°.

To determine **x**, we solve the linear inverse problem as successively described by *Purucker et al.* [1996, 2000], *Langlais et al.* [2004], and *Langlais and Purucker* [2007], which seeks to minimize the sum of squares of residuals, $\nu^T\nu$. We use the iterative conjugate gradient technique to solve the inverse problem. This leads to a set of possible solutions, i.e., successive magnetization distributions, each one associated with a unique misfit to the observations.

We monitor the evolution of $\sigma_{\mathbf{B}_j}$, the root mean square (RMS) difference between the observed and modeled magnetic fields, with respect to $\sigma_{\mathbf{M}_j}$, the RMS magnetization, as a function of iteration number j. These quantities are written as follows:

$$\sigma_{\mathbf{B}_j} = \sqrt{\frac{\sum_{i=1}^{N_{obs}} (\mathbf{B}_i^{obs} - \mathbf{B}_{i,j}^{mod})^2}{N_{obs}}} \tag{6}$$

and

$$\sigma_{\mathbf{M}_j} = \sqrt{\frac{\sum_{i=1}^{N_{dip}} \mathbf{M}_{i,j}^2}{N_{dip}}} \tag{7}$$

where $\mathbf{B}^{obs}$ and $\mathbf{B}_j^{mod}$ are the observed and predicted (by $\mathbf{M}_j$) magnetic field vectors, respectively, and N_{obs} is the number of measurements. The full series of σ_{B_j} and σ_{M_j} are denoted σ_B and σ_M.

The vector correlation coefficient is also calculated during the tests according to the following:

$$r_{B_j} = \frac{\sum(\mathbf{B}_j^{mod} - \overline{\mathbf{B}_j^{mod}}) \cdot (\mathbf{B}^{obs} - \overline{\mathbf{B}^{obs}})}{\sqrt{\sum(\mathbf{B}_j^{mod} - \overline{\mathbf{B}_j^{mod}})^2}\sqrt{\sum(\mathbf{B}^{obs} - \overline{\mathbf{B}^{obs}})^2}} \tag{8}$$

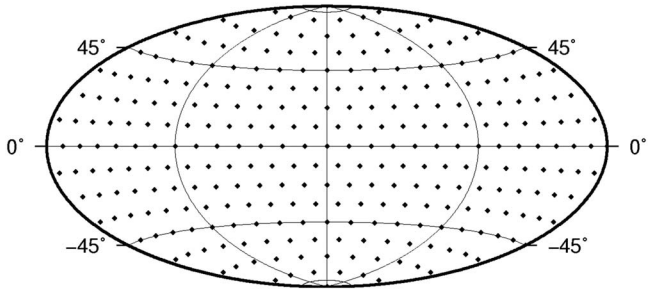

Figure 2. Example of a dipole mesh using the polar coordinate subdivision method for a dipole mesh parameter $n_d = 15$.

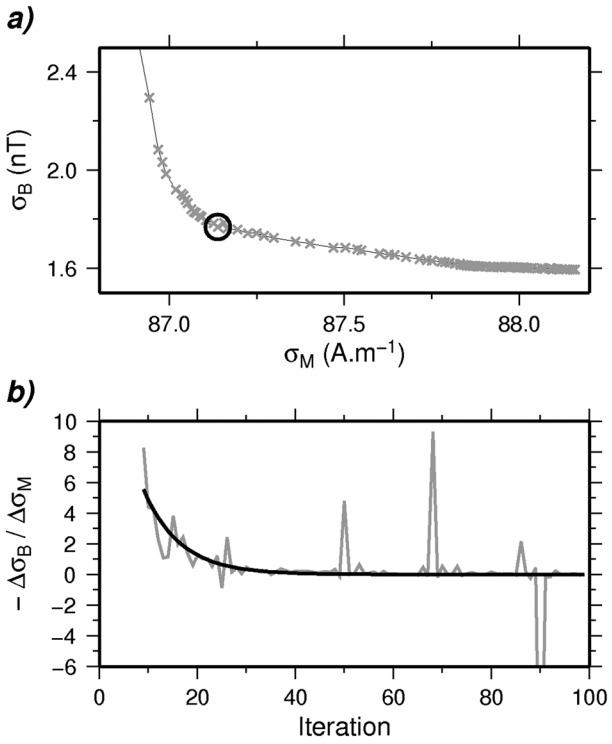

Figure 3. (a) Example of a trade-off curve between σ_B and σ_M for all iterations using synthetic data on grids. (b) $-\Delta\sigma_B/\Delta\sigma_M$ as a function of the iteration number (grey line), with exponential fit of its filtered curve (black line). The black circle in Figure 3a shows σ_B and σ_M for the iteration chosen using Figure 3b, see text for details. The synthetic data are composed of six regular grids at 300 km, 400 km and 500 km altitudes and at two different epochs (with one terrestrial year difference). The dipole mesh is located at 640 km depth with $n_d = 19$ (see section 4.2).

where $\mathbf{B}^{obs}$ and $\mathbf{B}^{mod}$ are the observed and modeled magnetic field vectors and $\overline{\mathbf{B}^{obs}}$ and $\overline{\mathbf{B}^{mod}}$ their spatial averages, respectively. An r_B value close to 1 means that the modeled and observed magnetic field patterns are alike. Given the large amount of observations compared to the number of dipoles (large number of degrees of freedom), a correlation coefficient larger than ~0.2 is statistically significant with 95% confidence [*Press et al.*, 1992].

We look for the iteration associated with low values in both σ_B and σ_M, for which the magnetization distribution satisfactorily explains the measurements without being unrealistically too energetic. This is illustrated in Figure 3a which shows a trade-off curve between σ_B and σ_M. The misfit to the observed magnetic field decreases while the magnetization increases with increasing iteration number. After iteration 1, σ_B rapidly decreases to a low value with a small increase of σ_M. The following iterations show a slowly decreasing σ_B but more rapidly increasing σ_M. Finally, σ_B approaches an asymptotic value while σ_M continues to increase. The solution is commonly chosen in the knee of the trade-off curve [*Gubbins*, 2004]. To select the optimal iteration, we look for the iteration number when the slope of the trade-off curve (Figure 3a) begins to flatten. The $-\Delta\sigma_B/\Delta\sigma_M$ curve can be very noisy but nonetheless shows a global decaying trend as a function of the iteration number (Figure 3b). We use a pseudo-Gaussian filter which eliminates the spikes, and we fit the filtered curve with an exponential function. In the example shown in Figure 3b, the correlation coefficient between the filtered and fitted curves is 0.99. The solution is chosen when the fitted curve reaches a fixed percentage of its maximum value, which we arbitrarily set to 10%. In Figure 3b this corresponds to $j = 27$, as highlighted by the black circle in Figure 3a. We also tested the result with a threshold value of 1%, leading to an optimal solution at $j = 44$. The magnetization RMS increases by 8.4%, while the RMS difference between observed and modeled magnetic fields only decreases by 0.35%, with correlation coefficients exceeding 0.99 between M_{27} and M_{44} and between B_{27}^{mod} and B_{44}^{mod}. This shows that additional iterations do not significantly improve the fit to the measurements while causing a significant increase of the magnetization, thus supporting our choice of selecting a smaller iteration number with a 10% threshold.

4. Validation

We test the TD-ESD method using synthetic measurements based on a scaled-to-Mercury geomagnetic field model. Measurements are mapped either on regular grids at different altitudes or at spacecraft positions. We evaluate the dependence of the misfit on the various parameters of the inversion, including the dipole mesh resolution and depth. We also estimate the altitude range where the resulting magnetic field can be adequately modeled.

4.1. Synthetic Data

A synthetic SH magnetic field model is generated by scaling an Earth's magnetic field model to Mercury's geometry and intensity, taking into account the planet's higher core to surface radii ratio and weaker

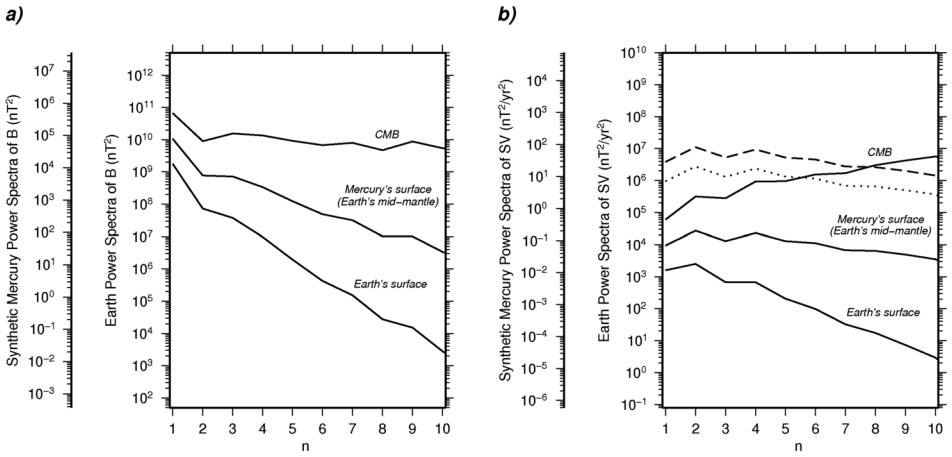

Figure 4. Power spectra of (a) the magnetic field and (b) the secular variation for the Earth (POMME4.1 model) and the synthetic scaled to Mercury model, with inside and outside *y* axes, respectively. For both plots the spectra are computed at three surfaces: Earth's surface, Mercury's surface corresponding to Earth's midmantle, and the CMB. Also shown on Figure 4b are the fast and superfast synthetic SV models at Mercury's surface (dotted and dashed lines, respectively).

magnetic field intensity. We use the POMME-4.1 internal field model (available at http://www.geomag.us/models/Pomme4/pomme-4.1.cof), an updated version of POMME-3.0 [*Maus et al.*, 2006], truncated to degree and order 10. First, the model is downward continued to some depth $R^h_\oplus$ inside the Earth's mantle, so that

$$\frac{R^c_\oplus}{R^h_\oplus} = \frac{R^c_M}{R_M} \tag{9}$$

where $R^c_\oplus$ is the radius of the Earth's core, and R^c_M and R_M are the core and surface radii of Mercury, respectively. This determines the magnetic field pattern that would be observed at Mercury's surface for such a field model. In equation (9) we use a Mercury core radius of 1800 km, within the range of values proposed by *Verhoeven et al.* [2009]. More recent studies proposed a core radius of about 2020 km [*Hauck et al.*, 2013; *Rivoldini and Van Hoolst*, 2013]. The choice of this value is however not critical as it is only used here as a geometric scale factor. Second, the Gauss coefficients are scaled by f with

$$f = \frac{g^0_{1M}}{g^0_{1\oplus}} \tag{10}$$

where $g^0_{1\oplus}$ is the axial dipole Gauss coefficient of the geomagnetic field model and g^0_{1M} is the corresponding coefficient of Mercury, taken as the average of models 5 and 6 of *Anderson et al.* [2010] from Mariner 10 and MESSENGER flybys (see their Table 1).

We use the same factor f to scale the geomagnetic SV to Mercury, corresponding to assuming SV correlation times [*Hulot and Le Mouël*, 1994] identical for Earth and Mercury. To establish a criterion for the SV detection time, we also consider larger SV by arbitrarily multiplying the scaling factor f by 10 and 20. In the following the three SV models are denoted normal, fast, and superfast. The scaling factors used are chosen only for testing the TD-ESD method and do not intend to simulate the actual temporal variation of the internal magnetic field at Mercury. They nonetheless give us some insight about the time interval that should be covered by the data in our TD-ESD inversion method, in order to properly recover the Hermean SV if it resembles that of our synthetic model.

The power spectra of the main field and its SV for the Earth and the corresponding synthetic spectra for Mercury are shown in Figure 4. As expected, the main field power spectrum at Earth's midmantle corresponding to Mercury's surface is steeper than at Earth's CMB but flatter than at Earth's surface. The field spectra at Earth's midmantle and at Mercury's surface show a dominant dipole. The quadrupole and the octupole have roughly the same energy. The SV spectra at Earth's midmantle and at Mercury's surface are rather flat, as opposed to blue at Earth's CMB and red at Earth's surface. We note that degrees 2 and 4 dominate the SV spectra at Earth's midmantle (Mercury's surface).

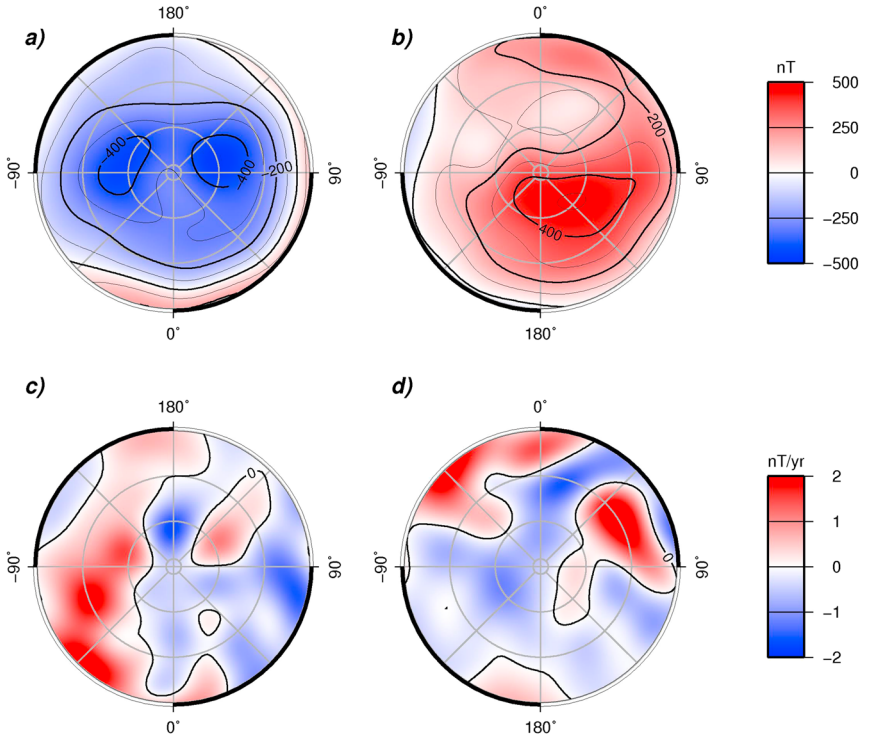

Figure 5. Synthetic magnetic field (a and b) and normal SV (c and d) at Mercury's surface in northern (a and c) and southern (b and d) polar views using a stereographic projection. Grid lines (grey) are drawn every 45° for longitude and every 30° for latitude.

Maps of the synthetic radial magnetic field and its normal SV at Mercury's surface are shown in Figure 5. The synthetic radial magnetic field varies between −488 and 512 nT, while the radial SV (normal case) varies between −1.7 and 2.65 nT/yr. Nonzonal main field contributions that are very strong at Earth's CMB [see *Christensen et al.*, 2010, Figure 1c] are rather weak at Earth's surface but would still be very evident if the dynamo was closer to Earth's surface as is the case for Mercury.

4.2. Ideal Case: Data on Regular Grids

We first test our TD-ESD method with synthetic data of purely internal origin on regular grids. This represents the ideal case where measurements are acquired uniformly and globally. These grids have constant latitude and longitude 2° increments. Three different altitudes above Mercury's surface (300, 400 , and 500 km) are considered, as well as two epochs (separated by 1 year), leading to six synthetic grids. Several dipole mesh parameters n_d values are tested, between 8 and 24. Different dipole mesh depths R_d are also considered, between 0 km and 1300 km.

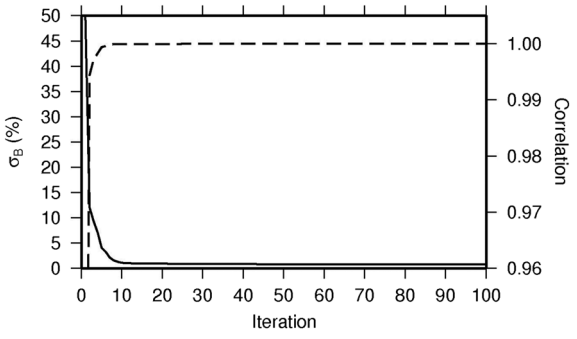

Figure 6. Relative misfit of the magnetic field vector (solid line, left axis) and the vector correlation coefficient (dashed line, right axis) versus iteration number.

In Figure 6 we show the relative misfit (i.e., σ_B divided by the initial RMS field σ_{B_0}) and the vector correlation coefficient as a function of the iteration number for n_d=19 and for R_d = 640 km, corresponding to the case presented in Figure 3. Both the relative misfit and the correlation coefficient reach asymptotic values rapidly. The misfit reaches 2% of the initial field RMS at iteration number 13. The correlation coefficient reaches its asymptote faster and exceeds 0.99 after iteration 2.

We use the scheme described in section 3.2 to choose the optimal solution at iteration

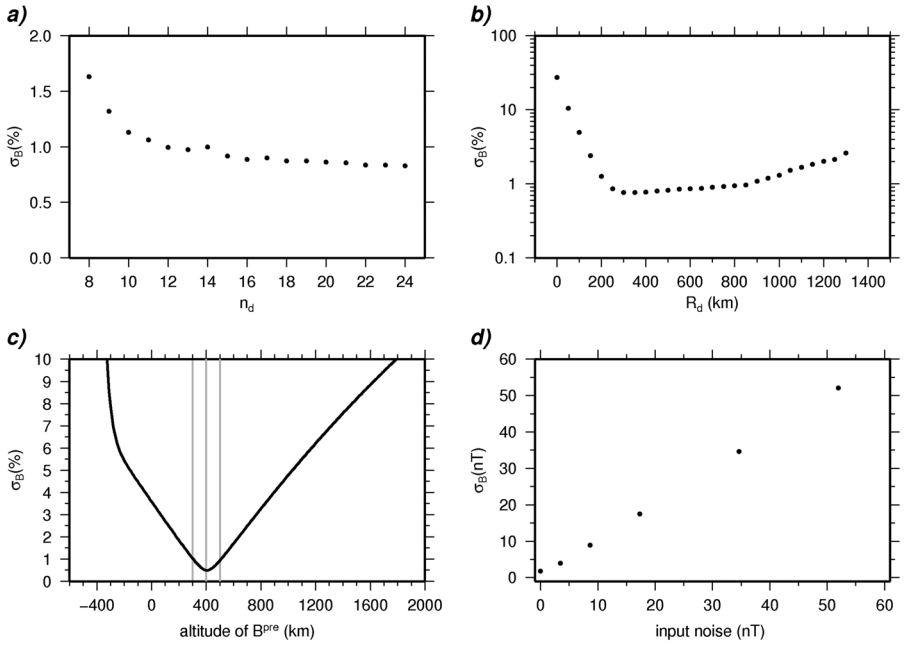

Figure 7. Relative magnetic field misfit as a function of (a) dipole mesh parameter n_d, (b) dipole mesh depth R_d, (c) modeled magnetic field altitude. The grey vertical lines in Figure 7c represent the input grids altitude. (d) The absolute misfit versus the input white noise amplitude. The dipole mesh is 640 km deep and the dipole mesh parameter is set to $n_d = 19$ unless specified. The synthetic data are predicted on six regular grids at 300 km, 400 km, and 500 km altitudes and at two different epochs with one terrestrial year difference.

number 27, as shown in Figure 3. For this solution, the relative misfit is 0.87% (1.79 nT) and the correlation coefficient is above 0.99. The synthetic normal SV is also recovered at Mercury's surface but with a degraded quality, with a relative misfit of 75% and correlation coefficient of 0.81. For the fast and superfast cases, the situation improves with relative misfit values of 8.1% and 5.8%, respectively, and the corresponding correlation coefficients exceed 0.99.

The sensitivity of the solution to the resolution of the dipole mesh is tested by varying n_d between 8 and 24 with R_d = 640 km (Figure 7a). The relative misfit decreases from n_d = 8 to 15, and then there is only slight changes for larger n_d values. Odd n_d values are preferred in order to keep a symmetric dipole distribution with respect to the equator. In the following, we use $n_d = 19$, which is a good balance between the computational cost (increasing with n_d) and the misfit to the measurements.

Next we test the impact of the dipole mesh depth choice on our results. Several R_d values are considered, from Mercury's surface down to 1300 km depth with a 50 km increment (Figure 7b). Three main trends are found. From the surface down to 250 km depth, relative misfit values rapidly decrease from 28% to 0.9%. Between 300 and 850 km depth, the misfit values are low and roughly constant, between 0.8% and 1%. Finally, for deeper dipoles the misfit values increase. From this test we conclude that the exact choice of R_d is not critical and that any depth between 300 and 850 km leads to comparably satisfactory solutions. We also note that this interval contains the 640 km depth value that we assumed to scale our synthetic SH model.

We further evaluate the altitude range at which the field can be reliably downward or upward continued (Figure 7c). The field is computed at different constant altitudes from −400 to 2000 km (10 km increment) on regular grids of 2° resolution from both the initial SH model and from the TD-ESD resulting model, assuming R_d = 640 km and n_d = 19. The lowest misfit between the SH and TD-ESD models is found as expected at 400 km altitude, which is the average altitude of the synthetic data grids. Between −300 and 1460 km altitudes the relative error is lower than 8%, and we consider this to be the altitude range at which the resulting model can be used to reliably map the magnetic field.

Finally, we also consider the effect of adding noise to the synthetic measurements (Figure 7d). We assume a white noise with different amplitudes. Resulting measurements are then inverted with the TD-ESD method, again using R_d = 640 km and n_d = 19. We observe a linear increase of the misfit values with increasing noise

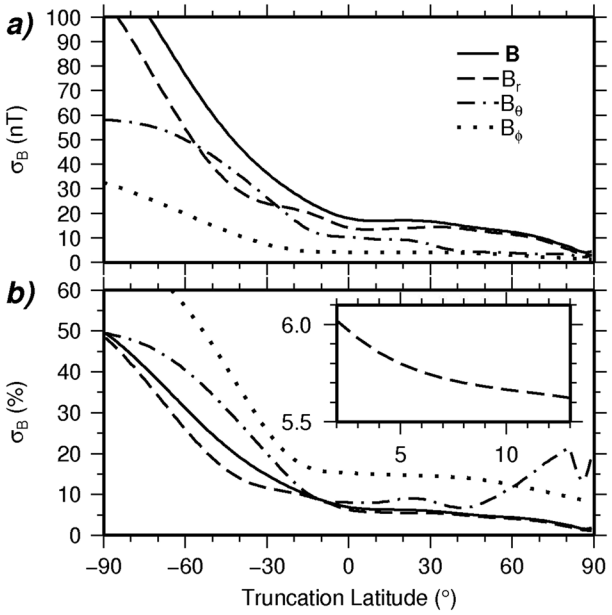

Figure 8. (a) Absolute and (b) relative misfits computed at constant altitude of 200 km, as a function of truncation latitude (see text), for |**B**| (solid line), B_r (dashed line), B_θ (dash-dotted line), and B_ϕ (dotted line). Inset in Figure 8b shows zoom-in for B_r around the transition from slow to rapid relative misfit change.

amplitude. Without any noise the misfit is 1.78 nT (relative misfit of 0.87%). This may be considered as the lowest bound of our method in the ideal case.

4.3. Realistic Case: Data Along Spacecraft Orbits

Next we test the TD-ESD method with synthetic measurements at MESSENGER spacecraft positions in order to simulate realistic conditions. During its primary mission, MESSENGER was on a very eccentric, near polar orbit, with a 200 km altitude periapsis at 60°N latitude. In the southern hemisphere the apoapsis was above 15,000 km. Magnetic field measurements were thus acquired both inside and outside the magnetosphere. Here we are interested in measurements inside the magnetosphere, i.e., where internal source contributions dominate. The orbital positions of the first sidereal day are selected using an external field proxy (defined in next section) and a 1000 km altitude limit and span a total time interval of 58.6 days between 23 March and 20 May 2011. The same exact sidereal day spacecraft positions are used twice with a 1 year time difference. This limits modeling errors related to differences in the position between the two sidereal days and allows focusing on the local temporal variation of the field instead. The SV is taken into account both during and between sidereal days.

In contrast to the ideal case where measurements are homogeneously distributed, measurements along MESSENGER orbits are available only above the northern hemisphere and along orbit paths. Because of this, σ_M and σ_B have to be carefully computed to minimize edge effects. Considering first which source dipoles should be included in the calculation of σ_M, we note that every dipole is constrained by a certain angular range of measurements above it and there is a latitude limit below which dipoles become less constrained. We looked at the number and the magnitude of elements in matrix D associated with each dipole and found that only dipoles from the north pole down to 30°N latitude are fully constrained, whereas dipoles south of 30°N are decreasingly constrained. In the following, σ_M is therefore computed using only dipoles north of 30°N. We emphasize that this critical latitude is used only to choose the iteration number. We also estimate the latitude range at which the magnetic field at constant altitude can be adequately modeled by the TD-ESD method, given the limited data coverage over the northern hemisphere. We apply the procedure for $n_d = 19$ and for $R_d = 640$ km. In Figure 8 we show relative and absolute σ_B values for the vector field and individual components as a function of the truncation latitude, i.e., the southernmost latitude considered for the computation of σ_B. The field is computed and compared to the SH model on a regular grid of 2° resolution at 200 km altitude. We choose the truncation latitude where the relative misfit begins to rapidly increase, i.e., at latitude 7°N as more clearly shown in the inset of Figure 8b.

We use the scheme described in section 3.2 to choose the optimal model solution. The trade-off curve between σ_B and σ_M (Figure 9) shows a similar behavior to that of the ideal case (Figure 3). First, σ_B decreases to about 10% of its initial value while σ_M increases slowly. Then σ_B and σ_M evolve together, until σ_B reaches a plateau while σ_M continues to increase. The raw, filtered, and exponentially fitted $-\Delta\sigma_B/\Delta\sigma_M$ curves are shown in Figure 9b. In this case the optimal solution is found at iteration 15, where the relative misfit is 2.59% and the correlation coefficient is larger than 0.99.

The input dipole mesh resolution n_d is tested (Figure 10a). We find an oscillatory dependence of the relative misfit for $n_d < 15$, which becomes nearly constant for larger n_d values. As for the ideal case, in the following

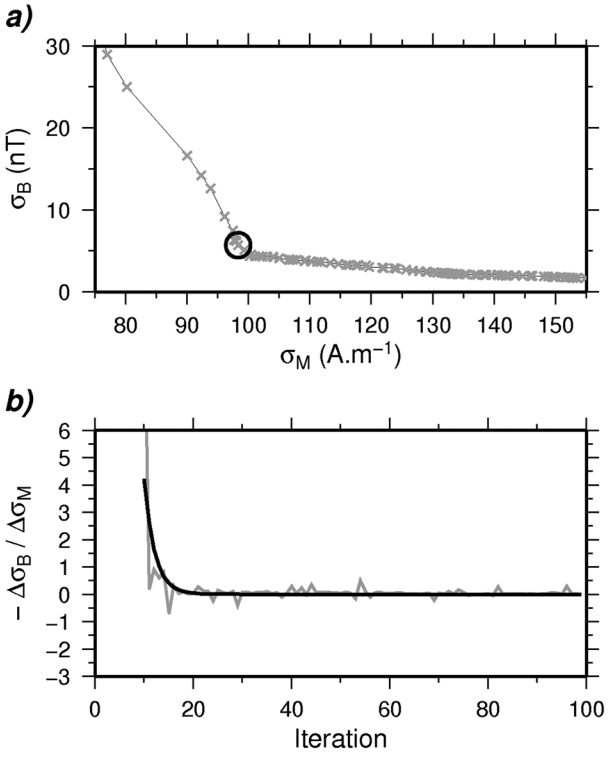

Figure 9. (a) Trade-off curve between σ_B and σ_M for all iterations. (b) $-\Delta\sigma_B/\Delta\sigma_M$ as a function of the iteration number, with exponential fit of its filtered curve (black line). The black circle in Figure 9a shows σ_{B_j} and σ_{M_j} for the chosen iteration using Figure 9b, see section 3.2 for details. The synthetic data is composed of two similar sidereal days by MESSENGER at two different epochs (an interval of 1 terrestrial year). The dipole mesh is located at 640 km depth with n_d = 19.

we choose $n_d = 19$. Several dipole mesh depths R_d are also considered. The misfit is larger for shallower dipole meshes (R_d between 0 and 150 km), while for deeper meshes the relative σ_B oscillates between 2 and 4% (Figure 10b). Contrary to the ideal case, we note that for deeper dipole meshes, relative misfit values remain low. The altitude range where the field can be downward and upward continued is evaluated. Retaining the relative difference between the SH field and that of the TD-ESD model to a maximum of 8% as acceptable, leads to an altitude range between 10 km and 970 km (Figure 10c), which is narrower than for the ideal case. The minimum relative misfit is reached at an altitude of 600 km, corresponding to the average altitude of the synthetic data. Note that as opposed to the ideal case, in the realistic case, σ_B is not symmetric about its minimum and a better fit is obtained for lower than for higher altitudes. Finally, we add to the measurements some noise. As for the ideal case, an almost linear dependency is found between σ_B and the amplitude of the white noise error added to the synthetic data (Figure 10d). Without any noise, the misfit is around 4.81 nT (equivalent to a relative misfit of 2.59%), which we consider as the lowest error bound of our method in the realistic case. In addition, we computed the influence of white noise on the altitude for which the field can be correctly described (see grey lines in Figure 10c). Adding 52 nT of noise to the synthetic data leads to an altitude range of 20–780 km, a decrease of roughly 200 km in the altitude range compared to the synthetic data with no noise. These results show that the altitude range where the field can be reliably downward and upward continued is not strongly sensitive to the noise.

Figure 11 compares maps of the radial component of the SV for the normal, fast, and superfast TD-ESD models, with the SH model from which synthetic data were generated all at the same altitude. We obtain some pattern agreement above the northern hemisphere only using the fast and the superfast models. Correlation coefficients are 0.54 and 0.77, respectively. Comparing Figures 11b and 11c with Figure 11d, we find some morphological agreement, e.g., positive SV structures at midlatitudes of longitudes 0–135°W and an intense negative structure at high latitudes around longitude 180°. Also note that the SV recovered with TD-ESD has an increasing zonal component with decreasing SV magnitude (from superfast to normal models). Overall however, the recovery of the SV pattern by the fast and superfast models is not satisfactory. The situation is even worse for the normal SV model (Figure 11a) where the correlation value is very low, only 0.07 above the northern hemisphere. Furthermore, the SV misfits of 1490%, 150%, and 80% for the normal, fast, and superfast models, respectively, are all too large. Above the southern hemisphere (not shown), the correlation coefficients are much lower, as expected. In summary, the TD-ESD is not able to properly recover the synthetic SV pattern and magnitude. We note, however, that both SV pattern and magnitude recovery improve with increasing SV magnitude in the data used. Therefore, since a larger SV magnitude is not expected for Mercury [*Philpott et al.*, 2014], a longer measurement time interval is needed in order to properly recover the Hermean SV.

These tests demonstrate that the TD-ESD can be used in the case of partial data coverage to successfully recover the morphology and intensity of the magnetic field of core origin. It is more difficult to correctly

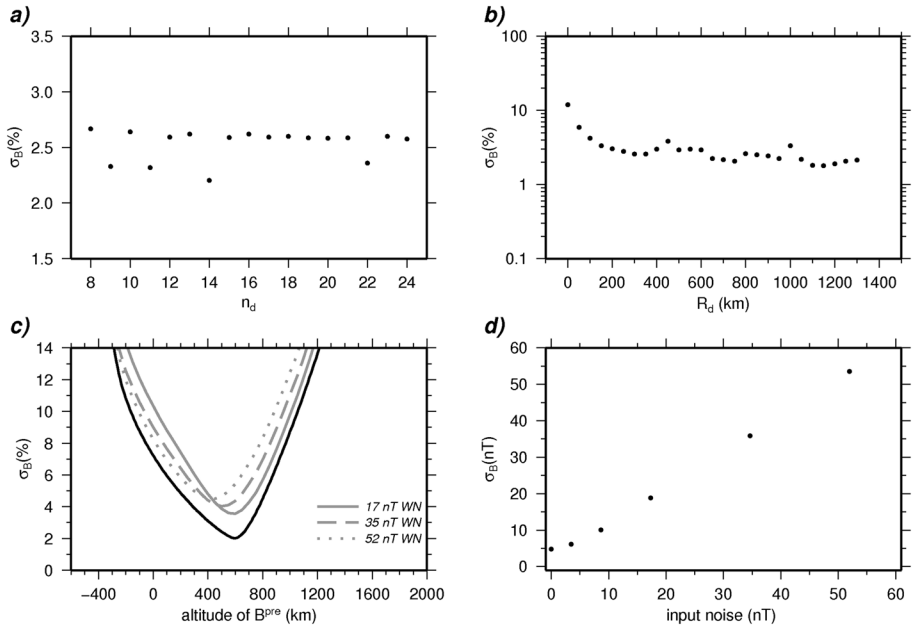

Figure 10. Relative magnetic field misfit as a function of (a) dipole mesh parameter n_d, (b) dipole mesh depth, and (c) modeled magnetic field altitude with (grey lines) and without (dark line) noise. Different levels of white noise are added: 17 nT (solid grey line), 35 nT (dashed grey line), and 52 nT (dotted grey line). (d) The absolute misfit versus the input white noise amplitude. The dipole mesh is 640 km deep and the dipole mesh parameter is set to $n_d = 19$ unless specified. Input data are predicted along MESSENGER orbits up to 1000 km altitude.

recover the secular variation, especially when it is slow. From these tests, we used in the following $n_d = 19$ and $R_d = 640$ km to produce maps of the Hermean magnetic field based on MESSENGER measurements, without solving for SV terms.

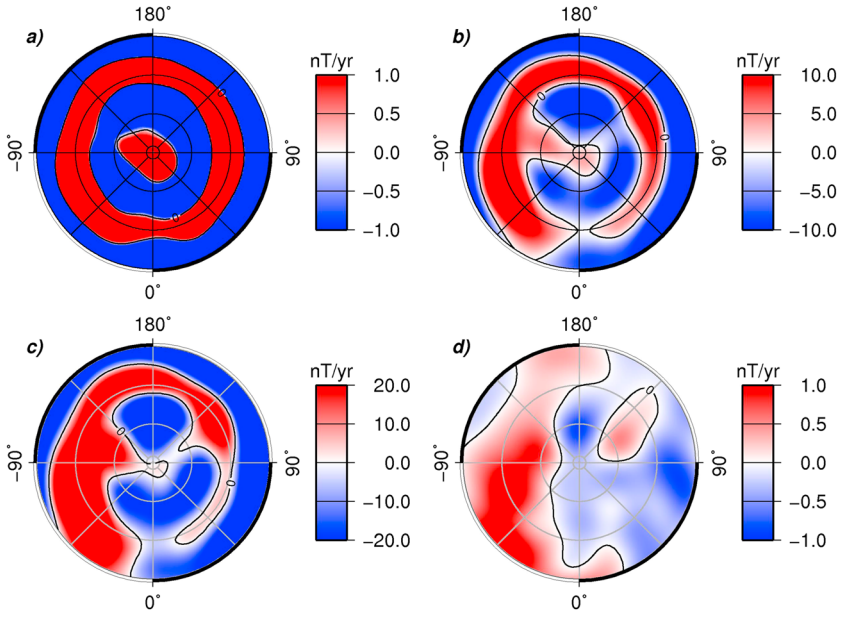

Figure 11. Radial SV recovered by TD-ESD from (a) normal, (b) fast, and (c) superfast models. (d) SH synthetic radial SV for the normal model (the fast and superfast models are scaled by 10 and 20, respectively). Figures show maps at 200 km altitude of the northern hemisphere using a stereographic projection. The dipole mesh is located at a depth $R_d = 640$ km with a dipole parameter $n_d = 19$.

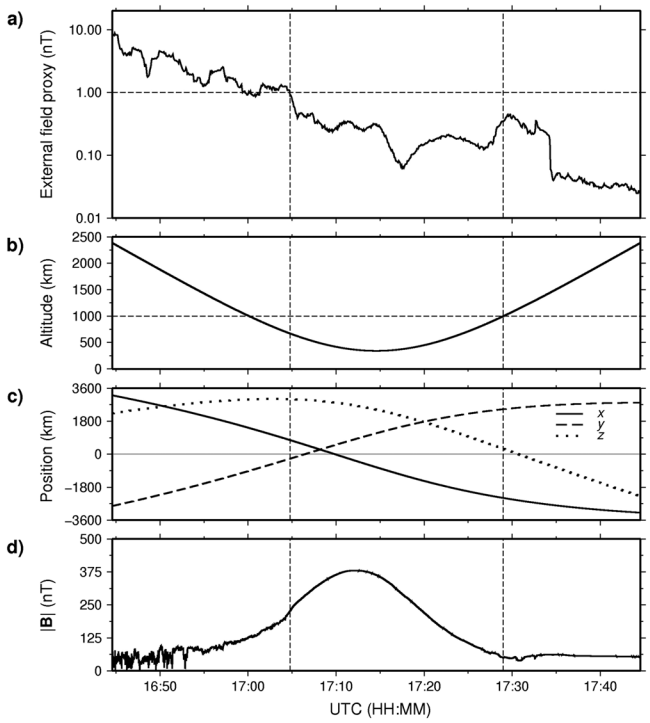

Figure 12. Orbit of MESSENGER spacecraft inside the magnetosphere for 17 April 2011. (a) External field Proxy, (b) spacecraft altitude from Mercury's surface in kilometers, (c) x,y,z MESSENGER orbit positions in MSO coordinates, and (d) intensity of the observed magnetic field in nT; all as a function of time. The proxy intensity value of 1 nT is used as the first criterion on data selection for the inversion (see horizontal line in Figure 12a). The altitude of 1000 km is used as a second criterion (see horizontal line in Figure 12b). Vertical dashed lines delimit the interval during which measurements are selected for this orbit.

5. Application to MESSENGER Measurements

We now consider the magnetic field of Mercury as measured by MESSENGER during the first four Hermean sidereal days. We define an external field proxy which is sensitive to the frequency content of the magnetic field measurements. It is used to select measurements less perturbed by the external component along MESSENGER orbit. First, a low-pass cosine time domain filter with 1 s width is applied to remove the high-frequency signal. We then use a 10 s moving average in order to smooth the filtered signal. The proxy contains the high-frequency signal that is obtained by subtracting the low-pass smoothed filtered signal from the measurements (Figure 12). High-frequency variations are usually present outside the magnetosphere and when crossing the magnetopause. We assume that proxy intensities lower than 1 nT correspond to MESSENGER being inside the magnetosphere or regions with low external activity. When the proxy values are larger than 1 nT, measurements are rejected. We show in Figure 12 the proxy for the magnetospheric transit on 17 April 2011. Proxy values larger than 1 nT are found on the dayside with positive X values in Mercury Solar Orbital (MSO) coordinate system. On the nightside the proxy remains lower than 1 nT. In addition, only measurements obtained below 1000 km altitude are kept. The magnetic field measurements acquired during the interval delimited by the vertical dashed lines are those selected for this orbit. We emphasize that the proxy is used only to identify the part of the data less perturbed of the external field, and the selected data are not filtered. As seen in Figure 12d, the field intensity shows a clear internal dipolar signature, with the field becoming more intense at lower altitudes and close to the pole.

Data are selected during 59 consecutive days (corresponding to 1 sidereal day of the planet) to get a complete azimuthal coverage in the Mercury Body Fixed (MBF) coordinate system. During this period, MESSENGER completed 117 orbits. The angular distance between two consecutive orbits at the equator is about 3°.

The ESD method is applied to the first four individual sidereal days. We do not solve for any temporal evolution, i.e., we assign the same epoch to all measurements of a given sidereal day. We do not remove a priori external magnetic field contributions. Maps of the chosen model of the Hermean magnetic field intensity

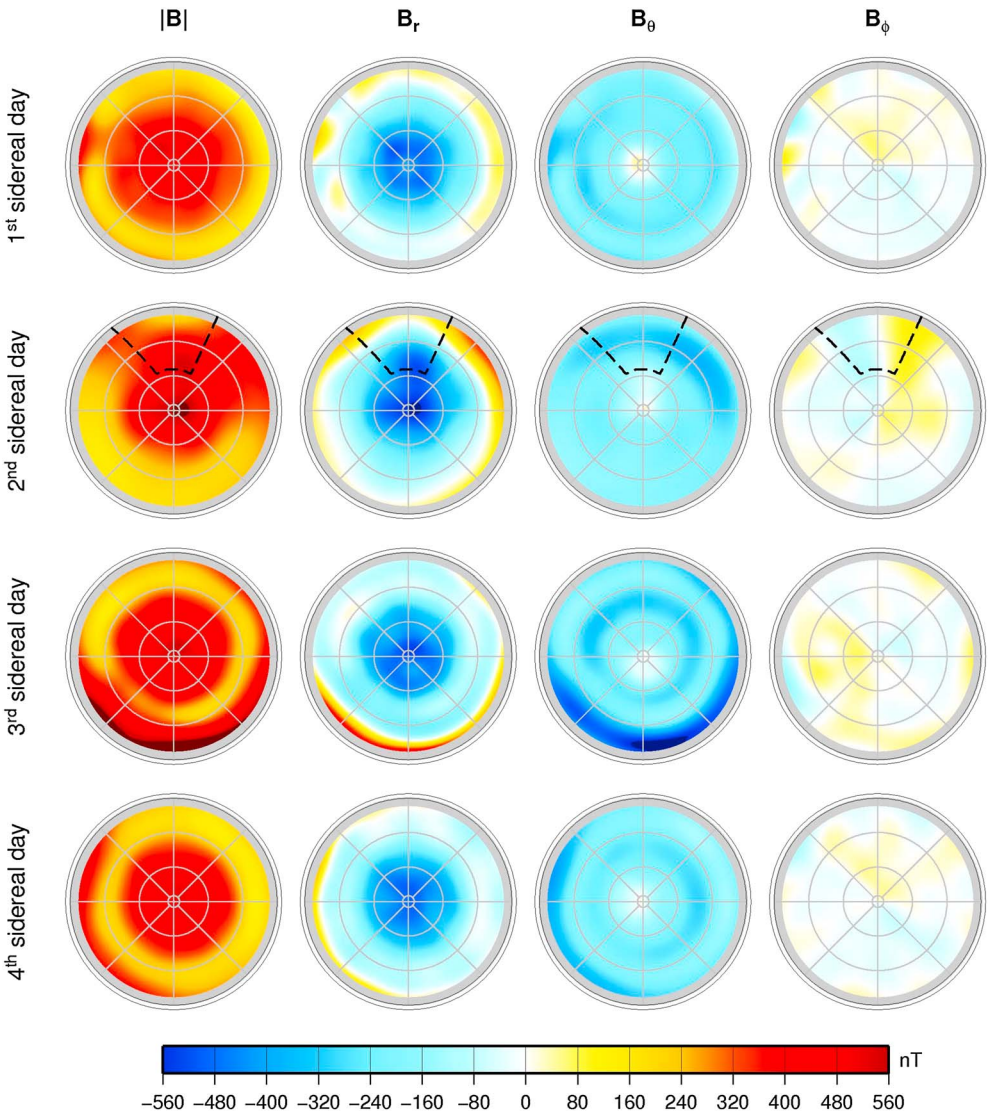

Figure 13. ESD-modeled magnetic field maps above the northern hemisphere of Mercury at 200 km altitude in MBF coordinates for the mean epochs of the first four MESSENGER sidereal days. The magnetic field unit is nT. Dashed lines in the second sidereal day indicate the measurement gap. Grid lines (grey) are drawn every 45° for longitude and every 30° for latitude. The maps are shown in stereographic projection. The 0° MBF longitude is toward bottom.

|**B**| and its spherical components, B_r, B_θ, and B_ϕ, are plotted for these four sidereal days at 200 km altitude in Figure 13. Only the northern hemisphere is shown because MESSENGER's eccentric orbit precludes reliable modeling of the internal field in the southern hemisphere (see Figure 8). The maximum absolute radial field B_r is located at the north pole region, and the magnetic equator ($B_r = 0$) is seen at low latitudes of the northern hemisphere. The B_θ component is negative everywhere. The B_ϕ component is much weaker than the other two components.

We observe, for all three components, small-scale features which seem to move around the rotation axis from one sidereal day to another; this is particularly clear for B_θ and B_ϕ. Because of the 3:2 spin-orbit resonance, the planet completes one solar day in three sidereal days (176 Earth days). During this time, every MBF longitude experiences all local time conditions. We thus interpret the rotating features as likely of external origin, related to the Sun varying position in the MBF frame. This hypothesis is supported by the comparison between the first and fourth sidereal days (with identical Sun positions) where the small-scale features exhibit similar spatial distributions.

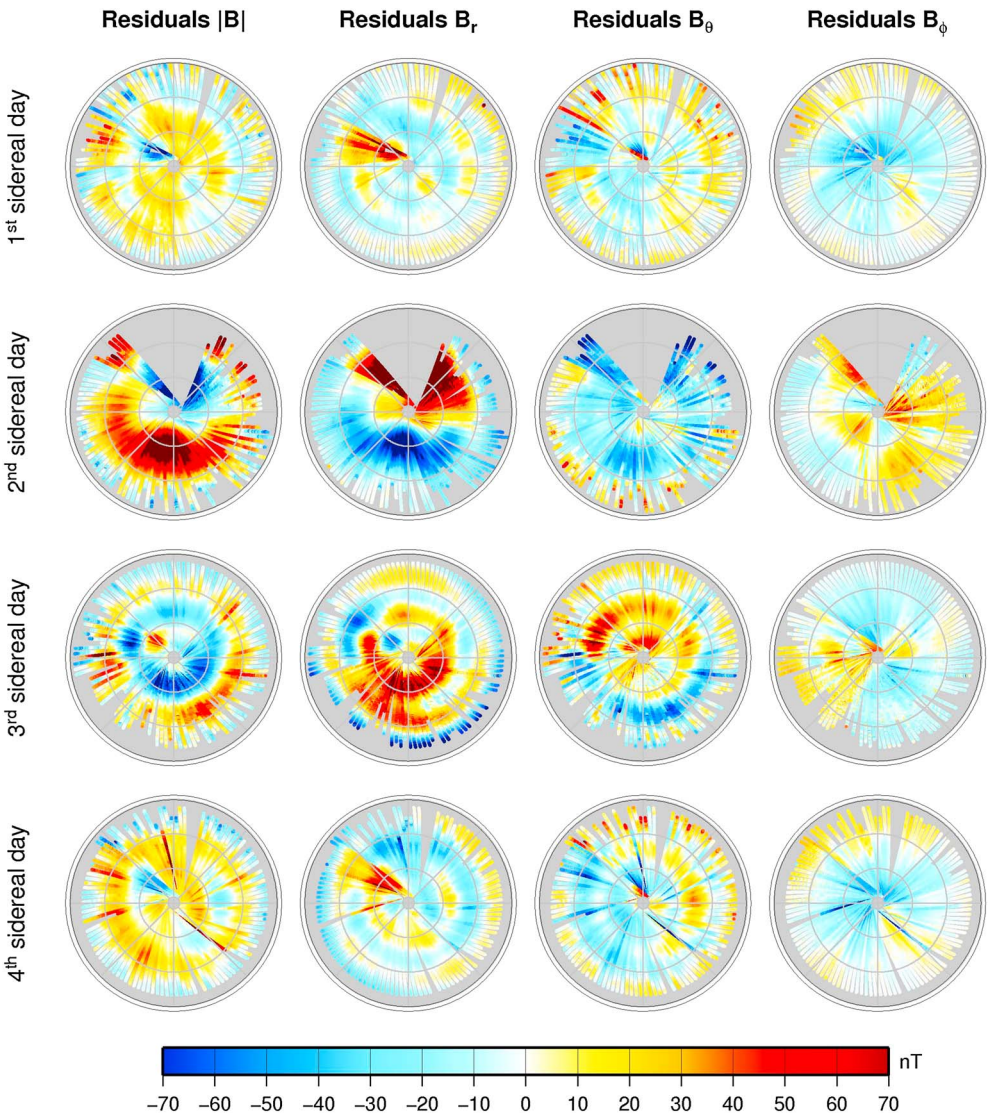

Figure 14. Magnetic field residual maps above the northern hemisphere of Mercury at 200 km altitude in MBF coordinates for the mean epochs of the first four MESSENGER sidereal days. Grid lines (grey) are drawn every 45° for longitude and every 30° for latitude. The maps are shown in stereographic projection. The 0° MBF longitude is toward bottom.

The corresponding residuals (unmodeled fields at spacecraft location) are shown in Figure 14 for the descending track. Strong positive B_r residuals are found north of 60°N, in the same region as the cusps identified by *Johnson et al.* [2012]. There are also orbit-to-orbit differences in the residuals related to the fact that during the 12 h interval between two successive tracks, the magnetospheric activity related to particles from solar wind and reconnection processes may drastically change [*Johnson et al.*, 2012]. During the second sidereal day, there is a measurement gap of about 20 orbits, during which the MAG instrument did not acquire data. This may explain the increased deviation of the maximum absolute radial field from the geographical pole (Figure 13). As with the field components, the residuals also display some repeating features after one complete solar day (or three consecutive sidereal days), which can again be associated with periodic external sources. Indeed, we observe very similar signatures for the first and fourth sidereal days, e.g., in the B_ϕ map the positive residuals at 45°E and at low latitudes between 135°E and 270°E. Similar rotating features can be observed for the other components as well (Figures 13 and 14). This means that when using only one sidereal day some external field contributions contaminate our model, whereas some other parts are not modeled and contribute to the observed misfit.

Table 1. Number of Observations Retained for Inversion, RMS of the Observed Field, Iteration Chosen, Relative Misfit, and Correlation Coefficients Between the Observed Field and the Model[a]

		Observed Field RMS (nT)					σ_B (nT)				Corr. Coeff.			
Sidereal Day	No. of Obs.	**B**	B_r	B_θ	B_ϕ	Iteration	**B**	B_r	B_θ	B_ϕ	**B**	B_r	B_θ	B_ϕ
1	86,134	275.3	238.9	133.4	28.7	23	31.8	16.4	18.0	20.5	0.98	0.99	0.96	0.71
2	68,971	291.2	252.1	141.3	35.7	7	57.6	46.4	27.5	20.2	0.94	0.95	0.94	0.83
3	89,947	281.2	242.0	139.6	32.2	14	42.2	27.9	24.2	20.4	0.96	0.98	0.93	0.78
4	88,649	292.5	258.7	132.7	31.8	14	41.0	22.4	24.7	23.8	0.97	0.99	0.92	0.65
One solar day	245,052	282.0	243.8	138.1	32.1	14	50.4	23.5	31.1	32.0	0.94	0.99	0.87	0.05

[a]The observed field RMS, the inversion misfit, and the correlation coefficient are given for the magnetic field vector and its spherical components B_r, B_θ, and B_ϕ. Values for one-solar-day model are also shown.

Table 1 shows statistics of the field models. The relative B_ϕ misfit is much larger than those of the other components because its magnitude is the lowest. The correlation coefficients are well above the level of statistical significance. The B_ϕ correlation coefficient is lower than those of the other components. Because the model is characterized by a field which is dominantly axisymmetric, the measured B_ϕ component is obviously less modeled using our approach, confirming that this measured component is likely dominated by the external field.

Misfit values also change from one sidereal day to another, but they tend to remain consistent with smallest values for the magnetic field intensity and the radial component, intermediate values for the latitudinal component, and highest values for the longitudinal component. We note that when the RMS of the observed field increases from one sidereal day to another, the corresponding residuals also increase. We also compare values for the first and fourth sidereal days, corresponding to similar Sun-Mercury orientations. The larger relative misfit values observed during the fourth sidereal day may be related to the larger RMS measured field and are probably related to stronger external field during that sidereal day (for instance, due to a possible increase of the solar activity).

We also apply the ESD method to the set of all measurements of the first three consecutive sidereal days during a total period of one solar day, again using the mean epoch as the common time. There are two main advantages over considering an individual sidereal day. First, there are (roughly) 3 times the number of observations, which may improve the signal-to-noise ratio provided that the signal we seek to model is coherent. Second, all local times are sampled during a solar day, meaning that the external field is measured 3 times at a given location under three different Sun-Mercury orientations, while the internal field remains practically constant. For this computation we do not attempt to recover the SV of the magnetic field, based on results in section 4. Moreover, external and internal fields vary differently with altitude and very small length scales at spacecraft altitudes are probably of external origin. It is therefore expected that the high-frequency external field contributions are significantly reduced in the one-solar-day model.

We use the technique described in section 3.2 to obtain the model. In general, the model changes very little with the iteration number (see supporting information). Residual statistics of the one-solar-day field model are also given in Table 1. The radial component is modeled with a misfit value of 23.5 nT (relative misfit of 9.6%) and a correlation coefficient exceeding 0.99. The misfit values for the one-solar-day B_θ and B_ϕ are larger than those for the individual sidereal days. This is interpreted as the one-solar-day field model being less contaminated by external field contributions than models based on individual sidereal days. The observed B_ϕ component is obviously poorly explained by the dominantly axisymmetric model, since σ_{B_ϕ} is the same order of magnitude as the observed RMS B_ϕ (see Table 1), indicating that this component is mainly of external origin.

We show in Figure 15 maps of the modeled magnetic field intensity and vector components for the first solar day of MESSENGER. The modeled field is much more axisymmetric than in the individual sidereal days. This axisymmetry can be quantified by the ratio of nonzonal to total modeled magnetic field, which is equal to 4.1% and 4.9% for the B_r and B_θ components, respectively. These ratios were obtained by considering the modeled magnetic field from the North Pole down to the truncation latitude 7°N over all longitudes. The much smaller values of B_ϕ compared to the other components are also consistent with a dominantly axisymmetric internal field. The maximum value of the (negative) radial component is found at a latitude exceeding 89°N.

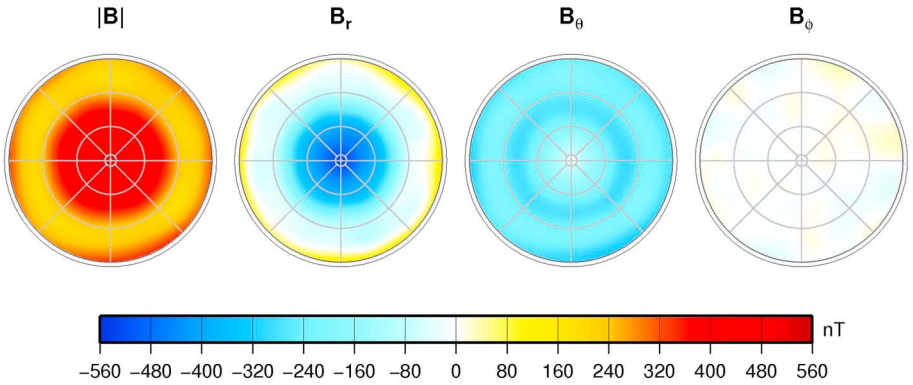

Figure 15. Stereographic projection maps of the magnetic field intensity |**B**| and its spherical components B_r, B_θ, and B_ϕ, for the first solar day of MESSENGER measurements. Maps represent the northern hemisphere of Mercury at 200 km altitude, in MBF coordinates. Grid lines (grey) are drawn every 45° for longitude and every 30° for latitude. The 0° MBF longitude is toward bottom.

The magnetic equator $B_r = 0$ is found in the northern hemisphere, and its position is between 6°N and 20°N. These results are qualitatively consistent with an axial and northward offset internal dipole pointing southward [*Anderson et al.*, 2012; *Johnson et al.*, 2012]. We discuss this point in the following section.

The axisymmetric dominance of the one-solar-day field model motivates examining the zonal radial field profile (Figure 16). The associated standard deviation (i.e., the RMS of the nonzonal field at each latitude) is also shown. Based on this profile, the mean magnetic equator $B_r = 0$ position is around 10°N latitude. This estimate has lower and upper bounds at 7.7° and 12.6°N latitude, respectively.

6. Discussion

6.1. MESSENGER One-Solar-Day Model

We now compare our field models with previously published models. We obtain misfits to the measurements of the vector **B** of ~40 nT for the individual sidereal days and 50.4 nT for the one solar day. These are larger than 10.7 nT obtained by *Alexeev et al.* [2010] and 20 nT by *Johnson et al.* [2012], but these models explicitly accounted for external field sources, which we do not do in the current approach. In the individual sidereal day inversions, some external fields may leak into our models. This effect is greatly reduced in the one-solar-day inversion, as evident from the larger misfit spatially correlated with the Sun position in the MBF frame and the null correlation coefficient between the observed and modeled B_ϕ component.

While the sidereal day models are dominated by zonal fields with some nonzonal contributions, the latter almost vanish when considering the one-solar-day model. We interpret these reduced nonzonal fields as being the signature of time-variable external fields. However, any nonaxisymmetric field of internal origin is expected to remain after the time-averaging of one solar day. We, therefore, conclude that the internal field of Mercury is strongly axisymmetric.

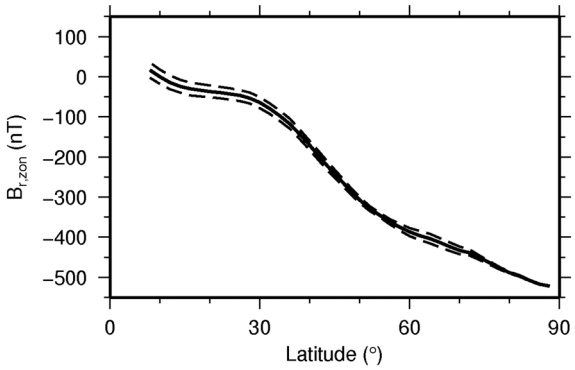

Figure 16. Zonal radial magnetic field (black solid line) with 1 standard deviation bounds (dashed lines, representing RMS nonzonal field), as a function of latitude. Only latitudes higher than 7°N (see Figure 8b) are shown.

A purely zonal field in general, and near-zero dipole tilt in particular, are in contradiction to Cowling's antidynamo theorem [*Cowling*, 1934]. For example, the purely axisymmetric field model of Saturn [*Connerney et al.*, 1982; *Cao et al.*, 2011] is enigmatic. Exotic mechanisms were proposed to explain it, most notably a conducting nonconvecting envelope surrounding the dynamo region of Saturn [*Stevenson*, 1980, 1982; *Schubert et al.*, 2004]. The Hermean internal field axysimmetry is therefore challenging for dynamo modeling.

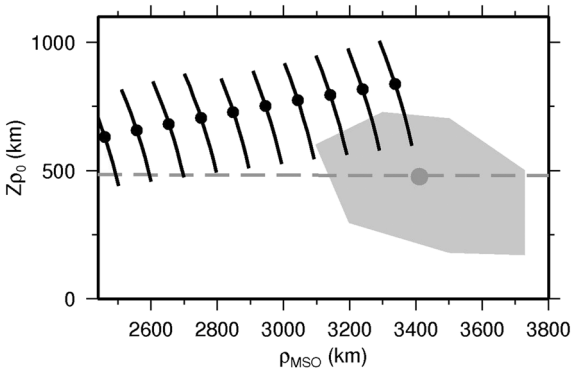

Figure 17. Cylindrical magnetic equator $B_\rho = 0$ axial displacement Z_{ρ_0} as a function of the distance to the planet rotation axis ρ, in MSO frame. Values were obtained from the one-solar-day model for different altitudes and longitudes (black lines). The black dots correspond to the average Z_{ρ_0} value for the corresponding altitude. Average (Z_{ρ_0}, ρ_{MSO}) pair for the low-altitude equator crossings of *Anderson et al.* [2012] is also plotted (grey dot). The grey region indicates where magnetic equator crossings were detected, and the grey dashed line is based on the estimate from the SH model of *Anderson et al.* [2012].

6.2. Magnetic Equator

Anderson et al. [2012] studied the position Z_{ρ_0} of the magnetic equator in cylindrical coordinates ($B_\rho = 0$). They identified the magnetic equator crossings directly from measurements and found an average axial displacement of $Z_{\rho_0} = 479 \pm 6$ km northward using the low-altitude crossings. The average magnetic equator position value for the high-altitude crossings is also around the same value, in agreement with a northward dipole offset. Figure 17 shows Z_{ρ_0} of our one-solar-day model as a function of the distance to the planet rotation axis ρ (in MSO cylindrical coordinates), for different altitudes and longitudes, in comparison with the values found by *Anderson et al.* [2012]. We consider only altitudes up to 1000 km, because relatively large misfit values were obtained for predicted magnetic field maps above that limit (see section 4.3).

For each altitude, our magnetic equator position varies with longitude. Our Z_{ρ_0} values partially overlap the crossings positions (grey region in Figure 17) observed by *Anderson et al.* [2012]. However, our average Z_{ρ_0} changes with ρ, in contradiction to the offset dipole model, although a constant Z_{ρ_0} could be consistent with the range of variability. Our average Z_{ρ_0} is larger than that of *Anderson et al.* [2012]. In the context of an offset dipole model, this larger Z_{ρ_0} would correspond to a larger g_2^0/g_1^0 ratio, which poses a challenge for numerical dynamos [*Cao et al.*, 2014; *Wicht and Heyner*, 2014].

6.3. Can Temporal Variations Be Modeled?

Using the TD-ESD method we demonstrate that a purely internal magnetic field can be correctly described in a limited region of the planet's neighborhood, with low misfits (below 5 nT) and close to unity correlation coefficients, even when only a partial data set is available (i.e., corresponding to the case of MESSENGER). This low misfit may be seen as the modeling limit of our method.

The case is different for the SV field. Using a global and regular data distribution and assuming SV characteristic timescales [*Hulot and Le Mouël*, 1994] identical to the Earth's (normal SV), we were unable to correctly model the SV when using synthetic measurements separated by 1 year. With this ideal data coverage, the fast and superfast SV models can nonetheless be correctly reproduced, with a correlation coefficient exceeding 0.99 and relative misfits below 8.1%. For a partial data coverage, even the superfast SV model cannot be adequately recovered: although the correlation coefficients are statistically significant, the patterns are not sufficiently similar and the misfit values are too large.

The characteristic SV timescale is inversely proportional to the magnetic Reynolds number R_m [*Christensen and Tilgner*, 2004; *Lhuillier et al.*, 2011; *Christensen et al.*, 2012], so assuming Earth-like characteristic timescales on Mercury is equivalent to assuming an Earth-like magnetic Reynolds number for Mercury. Our normal SV model corresponds to the same characteristic timescales for the Earth and Mercury, i.e., the same R_m. Even if the SV was 20 times higher (superfast SV model), i.e., a characteristic timescale 20 times lower and an R_m 20 times higher, we would not have resolved the SV magnitude correctly. We therefore conclude that the time required for our TD-ESD method to detect Mercury's SV is larger than $20R_m^{\oplus}/R_m^M$ years, where $R_m^{\oplus}$ and R_m^M are the magnetic Reynolds numbers of the Earth and Mercury, respectively. This seemingly negative result was obtained by modeling the SV with two similar sidereal days separated by one Earth year. In the future, we hope that modeling the SV with shorter sampling times and covering longer time periods may yield a more encouraging lower bound on the required time to detect the Hermean SV with a MESSENGER-like orbit.

7. Conclusion

In this study we introduce the Time-Dependent Equivalent Source Dipole method to model a dynamic magnetic field with partially distributed measurements. This method was validated using synthetic internal magnetic field measurements, both located on regular grids at different altitudes and only along MESSENGER orbits above the northern hemisphere. We designed and validated a scheme to select a unique and optimal iteration as a solution. We evaluated the performance of the method in recovering an internal field as a function of several input parameters, including the dipole mesh horizontal resolution and depth. We found that a horizontal resolution of 9.6° (n_d = 19) offers a satisfying compromise between the fit to the measurements and the computational cost. We chose a dipole mesh depth of 640 km, within the range proposed by *Verhoeven et al.* [2009]. We demonstrated that our results are weakly sensitive to the choice of dipole mesh depth (Figure 10b), and shallower depths [*Hauck et al.*, 2013; *Rivoldini and Van Hoolst*, 2013] may also be considered.

Next we determined the altitude range where the modeled magnetic field can be reliably upward or downward continued. This altitude range is −300 to 1460 km when using noise-free measurements ideally located on regular grids, and it is restricted to 10 to 970 km when using measurements along MESSENGER trajectories. For synthetic measurements with 52 nT of noise, the altitude range is 20 to 780 km, where the low bound is slightly higher than that of the noise-free measurements. More importantly, this partial data coverage does not degrade the quality of the model above the northern hemisphere. The minimum latitude at which the field can be reliably modeled by our TD-ESD method is 7°N. Our tests also showed that it is impossible to adequately recover the SV within two individual sidereal days separated by 1 year.

We then applied the ESD modeling scheme to the MESSENGER measurements during the first four consecutive sidereal days after the MAG instrument turned on (from 23 March 2011 to 13 November 2011). In order to reduce external magnetic field contributions, only measurements inside the magnetosphere were selected, using a proxy we defined. During these relatively short time intervals, we did not attempt to model the SV. Five models were computed and compared, one for each sidereal day plus one additional model for the first solar day of Mercury. For each of the first four sidereal day models, a dominantly axisymmetric field is observed. Small-scale features move around the rotation axis of the planet from one sidereal day to another, which we interpret as features of external origin related to the position of the Sun with respect to the planet. In the one-solar-day model (Figure 15) most of the nonaxisymmetric and small-scale features vanish, supporting their external origin. This latter field model has a more axisymmetric signature than in individual sidereal days, with a very small nonzonal to total magnetic field ratio. This is in agreement with previous studies [*Anderson et al.*, 2012; *Johnson et al.*, 2012]. We emphasize that using an inversion scheme which allows for nonaxisymmetric and small-scale features to be modeled, we recover a large-scale and dominantly zonal one-solar-day magnetic field model. This feature continues to provide a challenge for dynamo modeling [*Wicht and Heyner*, 2014].

The ESD method gives encouraging results for planetary magnetic field modeling. One advantage is the possibility to model the magnetic field of Mercury locally using a partial data set such as the one provided by MESSENGER and without any a priori regularization as previously used in SH models of Mercury [*Uno et al.*, 2009]. In the future, ESD will be applied to a larger set of MESSENGER measurements. This will lead to more accurate estimates for the field. Lower altitude measurements from the final phase of the MESSENGER mission may give new information about smaller length scales of the magnetic field that are not detectable at higher altitudes. Selecting orbits during quiet Sun activity conditions may reduce the external effects [*Anderson et al.*, 2013], but it would reduce significantly the number of observations and might also decrease the spatial and temporal coverage of the modeled magnetic field. Another possibility to overcome the external field contamination is to use an alternative parameterization or to extend the TD-ESD method by jointly modeling the internal and external sources. Our study helps to bring out all the difficulties met in using planetary-scale modeling methods when the data set is not globally distributed. It may guide in finding new approaches to constrain smaller scales of Mercury's magnetic field.

We argue that a strongly axisymmetric core field should be used as a constraint for modeling the Hermean dynamo. Our current view on the magnetic field of Mercury, based on limited spatial coverage, could change when more global measurements are available. The future BepiColombo mission of ESA/JAXA to Mercury [*Benkhoff et al.*, 2010] will map its magnetic field globally. For this future mission, global modeling methods

will likely be more suitable than partial coverage methods. However, the ESD method will still be appropriate to combine MESSENGER and BepiColombo measurements, in particular, in order to detect and estimate the time changes of the Hermean magnetic field between these missions.

Acknowledgments
We are grateful to Richard Holme and Chatherine C. Johnson for constructive reviews that significantly improved the paper. We also thank the Editor Sabine Stanley for the constructive comments. We thank Erwan Thébault, Michael Purucker, Melanie Drilleau, and Johannes Wicht for insightful discussions. A software to compute the three components of the magnetic field around Mercury following the model of our study is provided in the supporting information. The data used in this study are available from the NASA Planetary Data System at http://ppi.pds.nasa.gov. This work is partly funded through the ANR project MARMITE (ANR-13-BS05-0012) and PNP/ INSU/ CNRS program. M. A. Pais is supported by Fundação para a Ciência e Tecnologia (FCT: PTDC/CTE- GIX/119967/2010) and FEDER through the project COMPETE (FCOMP-01-0124-FEDER-019978).

References

Alexeev, I. I., et al. (2010), Mercury's magnetospheric magnetic field after the first two MESSENGER flybys, *Icarus*, *209*, 23–39, doi:10.1016/j.icarus.2010.01.024.

Amit, H., U. R. Christensen, and B. Langlais (2011), The influence of degree-1 mantle heterogeneity on the past dynamo of Mars, *Phys. Earth Planet. Inter.*, *189*, 63–79, doi:10.1016/j.pepi.2011.07.008.

Anderson, B. J., M. H. Acuña, D. A. Lohr, J. Scheifele, A. Raval, H. Korth, and J. A. Slavin (2007), The magnetometer instrument on MESSENGER, *Space Sci. Rev.*, *131*, 417–450, doi:10.1007/s11214-007-9246-7.

Anderson, B. J., M. H. Acuña, H. Korth, M. E. Purucker, C. L. Johnson, J. A. Slavin, S. C. Solomon, and R. L. McNutt (2008), The structure of Mercury's magnetic field from MESSENGER's first flyby, *Science*, *321*, 82–85, doi:10.1126/science.1159081.

Anderson, B. J., et al. (2010), The magnetic field of Mercury, *Space Sci. Rev.*, *152*, 307–339, doi:10.1007/s11214-009-9544-3.

Anderson, B. J., C. L. Johnson, H. Korth, M. E. Purucker, R. M. Winslow, J. A. Slavin, S. C. Solomon, R. L. McNutt, J. M. Raines, and T. H. Zurbuchen (2011), The global magnetic field of Mercury from MESSENGER orbital observations, *Science*, *333*, 1859–1862, doi:10.1126/science.1211001.

Anderson, B. J., et al. (2012), Low-degree structure in Mercury's planetary magnetic field, *J. Geophys. Res.*, *117*, E00L12, doi:10.1029/2012JE004159.

Anderson, B. J., C. L. Johnson, and H. Korth (2013), A magnetic disturbance index for Mercury's magnetic field derived from MESSENGER magnetometer data, *Geochem. Geophys. Geosyst.*, *14*, 3875–3886, doi:10.1002/ggge.20242.

Benkhoff, J., J. van Casteren, H. Hayakawa, M. Fujimoto, H. Laakso, M. Novara, P. Ferri, H. R. Middleton, and R. Ziethe (2010), BepiColombo—Comprehensive exploration of Mercury: Mission overview and science goals, *Planet. Space Sci.*, *58*, 2–20, doi:10.1016/j.pss.2009.09.020.

Cain, J. C., Z. Wang, C. Kluth, and D. R. Schmitz (1989), Derivation of a geomagnetic model to N = 63, *Geophys. J.*, *97*, 431–441.

Cao, H., C. T. Russell, U. R. Christensen, M. K. Dougherty, and M. E. Burton (2011), Saturn's very axisymmetric magnetic field: No detectable secular variation or tilt, *Earth Planet. Sci. Lett.*, *304*, 22–28, doi:10.1016/j.epsl.2011.02.035.

Cao, H., J. M. Aurnou, J. Wicht, W. Dietrich, K. M. Soderlund, and C. T. Russell (2014), A dynamo explanation for Mercury's anomalous magnetic field, *Geophys. Res. Lett.*, *41*, 4127–4134, doi:10.1002/2014GL060196.

Christensen, U. R. (2006), A deep dynamo generating Mercury's magnetic field, *Nature*, *444*, 1056–1058, doi:10.1038/nature05342.

Christensen, U. R., and J. Aubert (2006), Scaling properties of convection driven dynamos in rotating spherical shells and application to planetary magnetic fields, *Geophys. J. Int.*, *166*, 97–114, doi:10.1111/j.1365-246X.2006.03009.x.

Christensen, U. R., and A. Tilgner (2004), Power requirement of the geodynamo from ohmic losses in numerical and laboratory dynamos, *Nature*, *429*, 169–171, doi:10.1038/nature02508.

Christensen, U. R., and J. Wicht (2008), Models of magnetic field generation in partly stable planetary cores: Applications to Mercury and Saturn, *Icarus*, *196*, 16–34, doi:10.1016/j.icarus.2008.02.013.

Christensen, U. R., J. Aubert, and G. Hulot (2010), Conditions for Earth-like geodynamo models, *Earth Planet. Sci. Lett.*, *296*, 487–496, doi:10.1016/j.epsl.2010.06.009.

Christensen, U. R., I. Wardinski, and V. Lesur (2012), Timescales of geomagnetic secular acceleration in satellite field models and geodynamo models, *Geophys. J. Int.*, *190*, 243–254, doi:10.1111/j.1365-246X.2012.05508.x.

Connerney, J. E. P., N. F. Ness, and M. H. Acuna (1982), Zonal harmonic model of Saturn's magnetic field from Voyager 1 and 2 observations, *Nature*, *298*, 44–46, doi:10.1038/298044a0.

Connerney, J. E. P., M. H. Acuna, and N. F. Ness (1987), The magnetic field of Uranus, *J. Geophys. Res.*, *92*, 15,329–15,336, doi:10.1029/JA092iA13p15329.

Connerney, J. E. P., M. H. Acuna, and N. F. Ness (1991), The magnetic field of Neptune, *J. Geophys. Res.*, *96*, 19,023–19,042.

Cowling, T. G. (1934), The stability of gaseous stars, *Mon. Not. R. Astron. Soc.*, *94*, 768–782.

Dietrich, W., and J. Wicht (2013), A hemispherical dynamo model: Implications for the Martian crustal magnetization, *Phys. Earth Planet. Inter.*, *217*, 10–21, doi:10.1016/j.pepi.2013.01.001.

Dyment, J., and J. Arkani-Hamed (1998), Equivalent source magnetic dipoles revisited, *Geophys. Res. Lett.*, *25*(11), 2003–2006, doi:10.1029/98GL51331.

Emilia, D. A. (1973), Equivalent sources used as an analytic base for processing total magnetic field profiles, *Geophysics*, *38*, 339–348, doi:10.1190/1.1440344.

Gubbins, D. (2004), *Time Series Analysis and Inverse Theory for Geophysicists*, 272 pp., Cambridge Univ. Press, Cambridge, U. K.

Hauck, S. A., et al. (2013), The curious case of Mercury's internal structure, *J. Geophys. Res. Planets*, *118*, 1204–1220, doi:10.1002/jgre.20091.

Holme, R., and J. Bloxham (1996), The magnetic fields of Uranus and Neptune: Methods and models, *J. Geophys. Res.*, *101*, 2177–2200, doi:10.1029/95JE03437.

Hulot, G., and J. L. Le Mouël (1994), A statistical approach to the Earth's main magnetic field, *Phys. Earth Planet. Inter.*, *82*, 167–183, doi:10.1016/0031-9201(94)90070-1.

Johnson, C. L., et al. (2012), MESSENGER observations of Mercury's magnetic field structure, *J. Geophys. Res.*, *117*, E00L14, doi:10.1029/2012JE004217.

Katanforoush, A., and M. Shahshahani (2003), Distributing points on the sphere, *Exp. Math.*, *12*, 199–209.

Kutzner, C., and U. R. Christensen (2002), From stable dipolar towards reversing numerical dynamos, *Phys. Earth Planet. Inter.*, *131*, 29–45, doi:10.1016/S0031-9201(02)00016-X.

Langlais, B., and M. Purucker (2007), A polar magnetic paleopole associated with Apollinaris Patera, Mars, *Planet. Space Sci.*, *55*, 270–279, doi:10.1016/j.pss.2006.03.008.

Langlais, B., M. E. Purucker, and M. Mandea (2004), Crustal magnetic field of Mars, *J. Geophys. Res.*, *109*, E02008, doi:10.1029/2003JE002048.

Lhuillier, F., J. Aubert, and G. Hulot (2011), Earth's dynamo limit of predictability controlled by magnetic dissipation, *Geophys. J. Int.*, *186*, 492–508, doi:10.1111/j.1365-246X.2011.05081.x.

Margot, J. L., S. J. Peale, R. F. Jurgens, M. A. Slade, and I. V. Holin (2007), Large longitude libration of Mercury reveals a molten core, *Science*, *316*, 710–714, doi:10.1126/science.1140514.

Maus, S., M. Rother, C. Stolle, W. Mai, S. Choi, H. Lühr, D. Cooke, and C. Roth (2006), Third generation of the Potsdam Magnetic Model of the Earth (POMME), *J. Geophys. Res.*, *7*, Q07008, doi:10.1029/2006GC001269.

Mayhew, M. A. (1979), Inversion of satellite magnetic anomaly data, *J. Geophys.*, *45*, 119–128.

Ness, N. F., K. W. Behannon, R. P. Lepping, Y. C. Whang, and K. H. Schatten (1974), Magnetic field observations near Mercury: Preliminary results from Mariner 10, *Science*, *185*, 151–160, doi:10.1126/science.185.4146.151.

Ness, N. F., K. W. Behannon, R. P. Lepping, and Y. C. Whang (1975), The magnetic field of Mercury, 1, *J. Geophys. Res.*, *80*, 2708–2716, doi:10.1029/JA080i019p02708.

Philpott, L. C., C. L. Johnson, R. M. Winslow, B. J. Anderson, H. Korth, M. E. Purucker, and S. C. Solomon (2014), Constraints on the secular variation of Mercury's magnetic field from the combined analysis of MESSENGER and Mariner 10 data, *Geophys. Res. Lett.*, *41*, 6627–6634, doi:10.1002/2014GL061401.

Plagemann, S. (1965), Model of the internal constitution and temperature of the planet Mercury, *J. Geophys. Res.*, *70*, 985–993, doi:10.1029/JZ070i004p00985.

Press, W. H., S. A. Teukolsky, W. T. Vetterling, and B. P. Flannery (1992), *Numerical Recipes in C. The Art of Scientific Computing*, 2nd ed., Cambridge Univ. Press.

Purucker, M., D. Ravat, H. Frey, C. Voorhies, T. Sabaka, and M. Acuña (2000), An altitude-normalized magnetic map of Mars and its interpretation, *Geophys. Res. Lett.*, *27*, 2449–2452, doi:10.1029/2000GL000072.

Purucker, M., B. Langlais, N. Olsen, G. Hulot, and M. Mandea (2002), The southern edge of cratonic North America: Evidence from new satellite magnetometer observations, *Geophys. Res. Lett.*, *29*, 1342, doi:10.1029/2001GL013645.

Purucker, M. E., T. J. Sabaka, and R. A. Langel (1996), Conjugate gradient analysis: A new tool for studying satellite magnetic data sets, *Geophys. Res. Lett.*, *23*, 507–510, doi:10.1029/96GL00388.

Purucker, M. E., R. A. Langel, M. Rajaram, and C. Raymond (1998), Global magnetization models with a priori information, *J. Geophys. Res.*, *103*, 2563–2584, doi:10.1029/97JB02935.

Purucker, M. E., J. W. Head III, and L. Wilson (2012), Magnetic signature of the lunar South Pole-Aitken basin: Character, origin, and age, *J. Geophys. Res.*, *117*, E05001, doi:10.1029/2011JE003922.

Rivoldini, A., and T. Van Hoolst (2013), The interior structure of Mercury constrained by the low-degree gravity field and the rotation of Mercury, *Earth Planet. Sci. Lett.*, *377*, 62–72, doi:10.1016/j.epsl.2013.07.021.

Schubert, G., K. H. Chan, X. Liao, and K. Zhang (2004), Planetary dynamos: Effects of electrically conducting flows overlying turbulent regions of magnetic field generation, *Icarus*, *172*, 305–315, doi:10.1016/j.icarus.2004.06.007.

Smith, D. E., et al. (2012), Gravity field and internal structure of Mercury from MESSENGER, *Science*, *336*, 214–217, doi:10.1126/science.1218809.

Solomon, S. C., et al. (2001), The MESSENGER mission to Mercury: Scientific objectives and implementation, *Planet. Space Sci.*, *49*, 1445–1465, doi:10.1016/S0032-0633(01)00085-X.

Stanley, S., L. Elkins-Tanton, M. T. Zuber, and E. M. Parmentier (2008), Mars' paleomagnetic field as the result of a single-hemisphere dynamo, *Science*, *321*, 1822–1825, doi:10.1126/science.1161119.

Stevenson, D. J. (1980), Saturn's luminosity and magnetism, *Science*, *208*, 746–748, doi:10.1126/science.208.4445.746.

Stevenson, D. J. (1982), Reducing the non-axisymmetry of a planetary dynamo and an application to Saturn, *Geophys. Astrophys. Fluid Dyn.*, *21*, 113–127, doi:10.1080/03091928208209008.

Thébault, E., J. J. Schott, and M. Mandea (2006), Revised spherical cap harmonic analysis (R-SCHA): Validation and properties, *J. Geophys. Res.*, *111*, B01102, doi:10.1029/2005JB003836.

Uno, H., B. J. Anderson, H. Korth, C. L. Johnson, and S. C. Solomon (2009), Modeling Mercury's internal magnetic field with smooth inversions, *Earth Planet. Sci. Lett.*, *285*, 328–339, doi:10.1016/j.epsl.2009.02.032.

Verhoeven, O., P. Tarits, P. Vacher, A. Rivoldini, and T. van Hoolst (2009), Composition and formation of Mercury: Constraints from future electrical conductivity measurements, *Planet. Space Sci.*, *57*, 296–305, doi:10.1016/j.pss.2008.11.015.

Vilim, R., S. Stanley, and S. A. Hauck (2010), Iron snow zones as a mechanism for generating Mercury's weak observed magnetic field, *J. Geophy. Res.*, *115*, E11003, doi:10.1029/2009JE003528.

von Frese, R. R. B., W. J. Hinze, and L. W. Braile (1981), Spherical Earth gravity and magnetic anomaly analysis by equivalent point source inversion, *Earth Planet. Sci. Lett.*, *53*, 69–83, doi:10.1016/0012-821X(81)90027-3.

Whaler, K. A., and M. E. Purucker (2005), A spatially continuous magnetization model for Mars, *J. Geophys. Res.*, *110*, E09001, doi:10.1029/2004JE002393.

Wicht, J., and D. Heyner (2014), Mercury's magnetic field in the MESSENGER era, in *Planetary Geodesy and Remote Sensing*, edited by S. Jin, pp. 223–262, CRC Press., doi:10.1201/b17624-11.